

# Laning, Thinning and Thickening of Sheared Colloids in a Two-dimensional Taylor-Couette Geometry

Antonio Ortiz-Ambriz<sup>1</sup>, Sascha Gerloff<sup>2</sup>, Sabine H. L. Klapp<sup>2</sup>, Jordi Ortín<sup>1,3</sup>, and Pietro Tierno<sup>1,3,4\*</sup>

<sup>1</sup>*Departament de Física de la Matèria Condensada, Universitat de Barcelona, Barcelona, Spain*

<sup>2</sup>*Institut für Theoretische Physik, Technische Universität Berlin, Berlin, Germany*

<sup>3</sup>*Universitat de Barcelona Institute of Complex Systems (UBICS), Universitat de Barcelona, Barcelona, Spain and*

<sup>4</sup>*Institut de Nanociència i Nanotecnologia, Universitat de Barcelona, Barcelona, Spain*

(Dated: November 1, 2017)

We investigate the dynamics and rheological properties of a circular colloidal cluster that is continuously sheared by magnetic and optical torques in a two-dimensional (2D) Taylor-Couette geometry. By varying the two driving fields, we obtain the system flow diagram and report non-Newtonian velocity profiles along the colloidal structure. We then use the inner magnetic trimer as a microrheometer, and observe continuous thinning of all particle layers followed by thickening of the third one above a threshold field. Experimental data are supported by Brownian dynamics simulations that allow us to characterize the flow properties of the system. Our approach gives a unique microscopic view on how the structure of strongly confined colloidal matter weakens or strengthens upon shear, envisioning the engineering of future rheological devices at micro and nanometer scales.

PACS numbers: 82.70.Dd, 83.60.Rs

Understanding the dynamics of confined particulate systems under external deformations is relevant for many industrial and technological processes [1]. A classical yet versatile approach is based on the use of the Taylor Couette (TC) geometry, where complex fluids are confined and sheared between two coaxial cylinders [2, 3]. The possibility to independently rotate these cylinders has made this geometry a powerful tool to investigate the emergence of centrifugal instabilities, and how these flow perturbations lead to turbulence in a wide variety of soft matter systems, including foams [4, 5], granular materials [6–8], micellar [9] or polymeric solutions [10–12].

Equally appealing are the rheological properties of colloidal suspensions, complex viscoelastic fluids where the individual particles can be directly observed by optical means, and their interactions tuned by external fields [13]. As such, confocal microscopy of sheared bulk samples has revealed rich dynamics, including the emergence of thinning [14], thickening [15] or shear banding instabilities [16] in crystals [17] and glasses [18]. When confined by gravity to a two-dimensional (2D) plane, an ensemble of colloids is more difficult to shear, since particles tend to escape to the bulk due to compression or thermal fluctuations. Thus, the use of alternative driving methods, such as magnetic fields [19, 20] or optical tweezers [21, 22], may help creating compact clusters that can be confined and deformed by the applied drive. Recent experiments with optically confined microspheres have addressed the pressure exerted to the boundary [23] and the transmission of torque from the boundary to the center [24], while the rich and complex rheological properties of these systems remain unexplored. In addition, the interplay between shear and confinement gives rise to a host of new phenomena including buckling instabilities, transport via density waves, heterogeneities and defects that

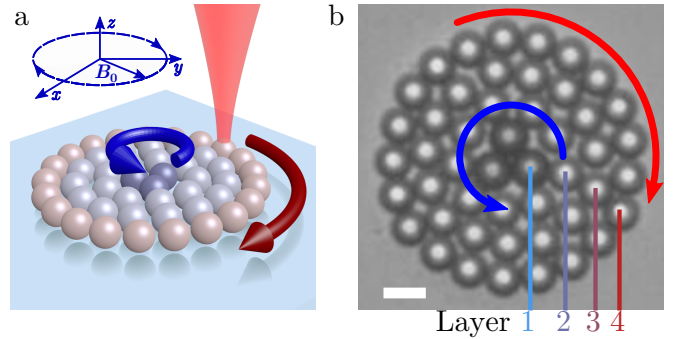


FIG. 1. (a) Scheme of the experimental system where a cluster of 48 microspheres is confined by 21 time-shared optical traps. The three inner particles are paramagnetic colloids that are subjected to an in-plane rotating magnetic field of amplitude  $B_0$ . Red (blue) arrow indicates the rotation direction induced by the optical (magnetic) field. (b) Microscope image of one colloidal cluster. Scale bar is  $5 \mu\text{m}$ , see also VideoS1 in [25].

have been mainly uncovered theoretically [21, 26–28].

In this Letter we investigate the dynamics and deformations of a circular colloidal cluster composed by interacting microspheres that are assembled and sheared via two independent driving fields. Even in the absence of shear, the particles arrange into four concentric layers, a generic effect in strongly confined systems [29]. Here, we use time-shared optical tweezers to assemble and rotate the outer particle layer. The other driving mechanism is a rotating magnetic field, which independently imposes a torque on a triplet of particles (trimer) located at the center of the system. In this 2D TC geometry, we observe non-Newtonian velocity profiles where neighboring layers of particles slide with each other cre-

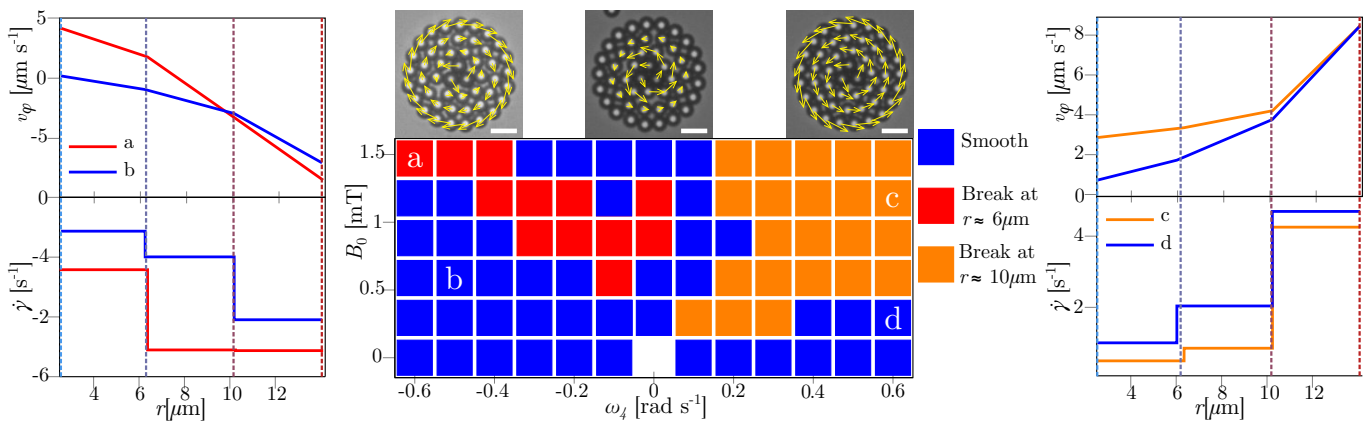


FIG. 2. Left and right columns: azimuthal velocity  $v_\varphi$  of the different layers (top) and shear rate  $\dot{\gamma}$  (bottom) versus distance  $r$  from the center of the cluster. Central column, top: microscope images of the colloidal cluster with the flow field superimposed as yellow arrows, see videos in [25]. Scale bar is  $10\mu\text{m}$  for all images. Bottom: flow diagram in the  $(\omega_4, B_0)$  plane illustrating the dynamic regimes observed, with smooth velocity profile (blue), a localized break at  $r = 6\mu\text{m}$  (red) or at  $r = 10\mu\text{m}$  (orange).

ating localized shear zones. By fixing the outer layer, we use the inner paramagnetic trimer as a microrheometer and thereby provide a realization of the original Couette experiment [30] on the colloidal length scale. Further, we observe that for a large magnetic torque, the fast spinning of the inner trimer generates a strong hydrodynamic flow and exerts a radial pressure pushing the third layer against the outer one. The corresponding change in the local densities of the layers manifests as a simultaneous shear thinning of the second layer and thickening of the third one. We use numerical simulations to calculate the local viscosities and the components of the stress tensor, obtaining consistent results with the experimental observations for the whole range of parameters explored.

The system geometry is schematically shown in Fig.1(a) for the counter-rotating case, see also VideoS1 in [25]. We use a binary mixture composed of polystyrene particles (diameter  $4\mu\text{m}$ , carboxylate modified from Invitrogen) and paramagnetic colloids (diameter  $4.5\mu\text{m}$ , M-450 Epoxy from Dynabeads). The iron oxide doping of the paramagnetic particles makes them slightly darker under brightfield microscopy, which allows us to distinguish them from the other particles when assembling the cluster. The particles are dispersed in highly deionized water (MilliQ, Millipore) and placed on a capillary chamber where they sediment due to a density mismatch. We assemble a circular cluster composed of 48 microspheres and radius  $R = 14.1\mu\text{m}$ , by trapping the outer 21 particles with an infrared laser ( $\lambda = 1064\text{nm}$ ) that is deflected with an acousto optic device (AOD). More details of the setup can be found in Ref. [25]. The AOD allows scanning the 21 traps in  $0.45\text{ms}$ , i.e. much faster than the typical self-diffusion time of the particles,  $\tau_B = 40\text{s}$ . Thus, the optical traps can then be considered as 21 independent harmonic potentials placed along the circle. The outer colloidal layer is either rotated with a constant an-

gular velocity  $\omega_4 \in \pm[0.1, 0.6]\text{rads}^{-1}$  when used in the TC geometry, or kept fixed ( $\omega_4 = 0\text{rads}^{-1}$ ) when using the inner trimer as a microrheometer. This trimer is created by placing three paramagnetic colloids at the cluster center and subjecting them to a rotating magnetic field with amplitude  $B_0$  and angular velocity  $\Omega$ ,  $\mathbf{B}(t) \equiv B_0[\cos(\Omega t)\hat{\mathbf{x}} - \sin(\Omega t)\hat{\mathbf{y}}]$ . The applied modulation induces the assembly of the paramagnetic particles due to time-averaged attractive magnetic interactions [31], and also induces a finite torque  $\mathbf{T}_m$  that forces the trimer to rotate at an angular velocity  $\omega_1$ . This torque results from the internal relaxation of the particle magnetization [32, 33] and can be calculated for the whole trimer as  $\mathbf{T}_m = V_c \mathbf{M} \times \mathbf{B} = V_c B_0^2 \chi_{eff}''(\Omega) \hat{\mathbf{z}} / \mu_0$ , where  $\mu_0 = 4\pi \cdot 10^{-7} \text{Hm}^{-1}$ ,  $V_c$  is the volume of the trimer, and  $\chi_{eff}'' = 0.18$  is the effective dynamic magnetic susceptibility, see Fig.1(b) in [25]. Thus, at a constant driving frequency of  $\Omega = 20\pi\text{rads}^{-1}$ ,  $\mathbf{T}_m \sim B_0^2$ , the amplitude of the rotating magnetic field is used to vary the rotational motion of the inner trimer.

Using video-microscopy, we measure the polar coordinates  $(r_i, \varphi_i)$  of each particle  $i$  with respect to the center of the cluster. We then obtain the average angular velocity per layer  $n$  as  $\omega_n = \langle N_n^{-1} \sum_i^{N_n} \omega(\mathbf{r}_i) \rangle$ , where the summation counts only the  $N_n$  particles within the respective layer, Fig.1(b). From these data, we calculate the azimuthal flow velocity,  $v_\varphi(r) = \langle \omega(r) \rangle r$  and the corresponding shear rate,  $\dot{\gamma}(r) = \partial(v_\varphi(r)) / \partial r$ .

In the central panel of Fig. 2 we show the complete flow diagram of our system obtained by varying the angular velocity  $\omega_4$  of the outer shell and the amplitude  $B_0$  of the applied magnetic field. We classify the different dynamical phases in terms of the velocity profiles and corresponding shear rates as they vary along the radial direction. Due to the strong confinement of our colloidal cluster, we never observed particle exchange between the

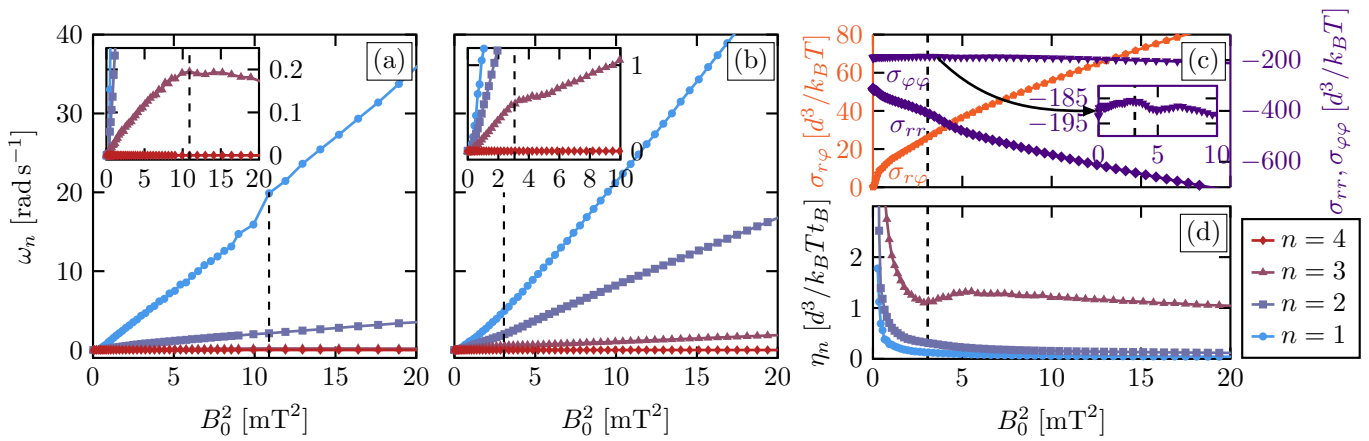


FIG. 3. (a,b) Time averaged angular velocities  $\omega_n$  for different layers  $n$  versus squared amplitude of the applied field  $B_0^2$  obtained from experiments (a) and Brownian dynamics (BD) simulations (b). Here the magnetic torque  $T_m \sim B_0^2$ . In both cases, the inset illustrates enlargements of the main graphs. (c) The three components of the stress tensor,  $\sigma_{r\phi} = \sigma_{\phi r}$  (orange),  $\sigma_{rr}$  and  $\sigma_{\phi\phi}$  (purple) versus  $B_0^2$  from BD simulations, the inset shows a zoom on  $\sigma_{\phi\phi}$ . (d) Viscosity  $\eta_n$  of the different layers  $n$  versus  $B_0^2$  from BD simulations. The dashed black line indicates the threshold fields  $B_c^2$ .

layers. Thus, our system does not display swirls and large scale rearrangements as observed in other sheared granular systems in two and three dimensions [6, 34–36]. However, the colloidal layers generate periodic corrugations that slide past each other during their relative motion. The strong confinement favors the fitting of particles of one layer in the interstices generated by the colloids of the neighboring layers. The size difference between the magnetic and non magnetic particles and the circular confinement frustrates ordering, and incommensurability effects between the different colloidal layers become important. Thus, depending on the directions and amplitudes of the shearing torques, the system may show layers that slip and others that temporary lock to each other, resulting in a non-Newtonian velocity profile. In order to characterize the different dynamical regimes, we plot the time-averaged azimuthal velocity per layer and the corresponding jump in the shear rate, some examples are shown in the left and right panels of Fig.2. In particular, we classify as "smooth" (blue regions in Fig.2) velocity profiles that lead to a jump in the shear rate smaller than a given threshold, in this case  $|(\dot{\gamma}_i - \dot{\gamma}_{i+1})/(\min_{\dot{\gamma}} - \max_{\dot{\gamma}})| \leq 0.15$ . On the contrary, in the red and orange regions the system displays velocity profiles with a strong discontinuity, leading to a pronounced jump ( $> 0.15$ ) in the shear rate. This shear-induced breakage is usually observed when there is no dominant driving mechanism, as opposed to when either the driving of the inner or outer layer is much stronger than the other. The breakage can be localized either between the first and the second layer ( $r = 6\mu\text{m}$ ) or the second and third layer ( $r = 10\mu\text{m}$ ). The first case occurs in the counter-rotating situation, when the inner trimer is able to drag the second layer of particles in opposite

direction than the outer layer, and the cluster inevitably breaks in pairs of counter-propagating colloidal domains (VideoS1 in [25]). In the co-rotating case, the breakage rather localizes close to the outer layer, as this colloidal shell has a stronger capability to drag nearest layers. The third layer is mainly driven by the fourth one, while the second has a reduced angular speed as it also tries to follow the rotating magnetic triplet. When the first and fourth layer have the same angular velocity ( $\omega_1 = \omega_4$ ), the system displays a Poiseuille like flow profile.

We will now focus on the central region of the flow diagram in Fig.2, where we keep the outer layer fixed ( $\omega_4 = 0$ ) and continuously rotate only the inner trimer. In Fig.3(a) we show experimental measurements of the average angular velocities of the four colloidal layers versus the square of the magnetic field up to  $B_0^2 = 20\text{mT}^2$ . Above a depinning threshold  $B_0 = 0.6\text{mT}$ , below which all particles are at rest, the trimer starts rotating and shows an angular velocity that increases linearly with  $B_0^2$ , up to a threshold field strength  $B_c = 3.3\text{mT}$ . At  $B_c$  we can see a sharp jump in the angular velocity of the trimer, where the mobility, i.e. slope of  $\omega_1$ , remains constant. Further, we observe that the slope of  $\omega_3$  reveals an abrupt decrease as the magnetic torque applied to the trimer increases, inset in Fig.3(a). As we will show later, this behaviour is related to a transition from "thinning" to "thickening" at  $B_c$ . Above  $B_c$  the fast spinning of the trimer generates a strong hydrodynamic flow that lubricates the region between the first and the second layer, see also VideoS5 in [25]. Thus, we find an overall thinning of the trimer viscosity for  $B_0 > B_c$ . This flow also pushes the third layer of particles towards the outer one, increasing the local packing density and reducing the effective mobility of this layer. This leads to an abrupt

transition to thickening as seen in the third layer at a critical field strength  $B_c$ .

In order to access the viscosity of all the layers and the system shear stresses, we perform 2D Brownian dynamics simulations of a binary mixture of charged colloids partially confined by harmonic potentials and paramagnetic colloids [25]. Taking into account hydrodynamic effects on the Rotne-Prager level, the overdamped equation of motion for the position  $\mathbf{r}_i$  of each colloid  $i$  is given by

$$\frac{d\mathbf{r}_i}{dt} = \sum_j \left( \underline{\underline{\mu}}_{ij}^{TT} \mathbf{F}_j + \underline{\underline{\mu}}_{ij}^{TR} \mathbf{T}_j \right) + \mathbf{\Gamma}_i(t), \quad (1)$$

where  $\underline{\underline{\mu}}_{ij}^{TT}$  and  $\underline{\underline{\mu}}_{ij}^{TR}$  are the mobility matrices due to translation-translation (TT) and translation-rotation (TR) couplings. The total force on the particle  $j$  is given by  $\mathbf{F}_j = \sum_{k \neq j} \mathbf{F}_{pp}(\mathbf{r}_{kj}) + \mathbf{F}_T(\mathbf{r}_j, t)$ , and is due to the particle-particle interaction ( $\mathbf{F}_{pp}$ ) and the optical traps ( $\mathbf{F}_T$ ), see [25] for more details. The torque acting on the paramagnetic particles is given by  $\mathbf{T}_j$ ,  $\mathbf{\Gamma}_i$  is a random force, stemming from random displacements with zero mean and variance  $2D_0\delta t$ , and  $D_0 \approx 0.4\mu\text{m}^2/\text{s}$  is the experimentally measured diffusion constant. The simulation time scale is set to the Brownian time  $\tau_B = d^2/D_0 \approx 40\text{s}$ , while the discrete time step is  $\delta t = 10^{-6}\tau_B$ .

The results of our theoretical model are shown in Fig.3(b), and placed on the same axis as the experimental data in Fig.3(a). We find that the model allows to qualitatively capture the dynamic features observed in the experiments. From the simulation results, the threshold field strength is observed earlier at  $B_c = 1.96\text{ mT}$ , which is of the same order of magnitude as in the experiment. Moreover, the simulations allow us to access all the rheological quantities of interest such as the shear viscosity of each layer,  $\eta_n = \sigma_{r\varphi}/\dot{\gamma}_n$  and the components of the stress tensor,  $\sigma_{rr}$ ,  $\sigma_{\varphi\varphi}$  and  $\sigma_{r\varphi} = \sigma_{\varphi r}$ . The shear viscosities of each inner colloidal layer are plotted as a function of  $B_0^2$  in Fig.3(d), and illustrate the continuous thinning of the first three layers as well as the thickening of the third one above  $B_c$ . We note that, being fixed by the optical tweezers ( $\omega_4 = 0$ ), the viscosity of the outer layer diverges and thus it is not reported in Fig.3(d). The same hold for the inner layers for  $B_0 \rightarrow 0$ , being pinned to the outer one. The transition at  $B_c$  is also reflected in all components of the stress tensors shown in Fig.3(c). In particular, the shear stress ( $\sigma_{r\varphi}$ ) displays an increase in the slope at  $B_c^2$ , and subsequent decrease at high magnetic field strengths, corresponding to the shear thinning and thickening respectively. The two diagonal components of the stress tensor decrease as the field increases, corresponding to an increase of the radial-  $P_r = -\sigma_{rr}$  and azimuthal pressure  $P_\varphi = -\sigma_{\varphi\varphi}$ . The shear thickening at  $B_c$  is accompanied by a steep increase of  $P_r$ , which is resolved subsequently.

While the dynamic transition at  $B_c$  appears to be

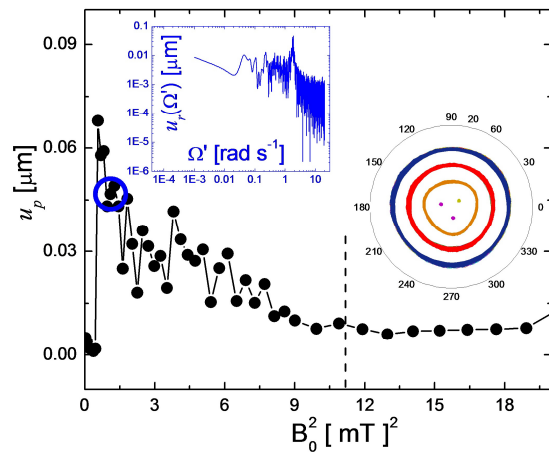


FIG. 4. Amplitude of the radial deformation  $u_p$  versus square of the magnetic field  $B_0^2$  for a fixed outer layer of particles ( $\omega_4 = 0$ ). Left inset: power spectrum of the elastic deformations measured for  $B_0^2 = 1.1\text{ mT}^2$ . Right inset: corresponding polar plot in the reference frame of the trimer of the particle trajectories showing the threefold tidal wave.

sharp in terms of the different rheological quantities, we find in the experiments that the cluster shows a continuous decrease in the amplitude of the radial distortions induced by the rotating trimer. Given the non-circular shape of the trimer, the particles from the second layer are forced to periodically enter and exit its interstitial regions. The induced deformation thus appears in form of a threefold tidal wave as shown in the small polar plot in Fig.4. To characterize these elastic deformations, we measure their amplitude as a function of the magnetic field strength in the Fourier space and in the reference frame of the trimer as,  $u_r(\Omega') = N_2^{-1} \sum_{j=1}^{N_2} T^{-1} \int_0^T \exp[3i(\Omega't - \varphi_j)] r(\varphi_j, t) dt$ , where  $r(\varphi_j, t)$  is the distance of the  $N_2$  particles composing the second layer and located at an angle  $\varphi_j$  in the reference frame of the trimer. In Fig.4 we plot the measured peak of  $u_r(\Omega')$ , namely  $u_p = \max[u_r(\Omega'), \Omega' \in \mathbb{R}]$ , as a function of  $B_0^2$  and in the upper left inset the corresponding  $u_r(\Omega')$  for one exemplary  $B_0$ . For small field strengths ( $B_0^2 < B_c^2$ ), the radial path of the particles in the second layer is deformed by the rotating trimer. After a transient regime, the amplitude of the deformation stabilizes to a stationary value where the relative speed between the  $N_2$  composing particles approaches zero. We further note that, being in the Stokes regime, the decoupling of the dynamics along the radial and azimuthal directions is effectively possible, and thus the emergence of two different types of dynamic transitions sharp and continuous, along either direction, respectively.

To conclude, we have realized a colloidal microrheometer based on the combined action of magnetic and optical torques. When sheared in a TC geometry, the inner col-

loidal layers show different dynamical regimes with velocity profiles that deviate from the simple Newtonian case, and reflect the discrete, granular-like nature of the system. By fixing the outer ring, the inner trimer allows exploring the rheological properties of the system inducing solidification and liquefaction of closed particle rings. The present approach may be used as an effective microrheological tool to explore the viscoelastic properties of complex fluids. This could potentially include biological media confined between the magnetic trimer and the optically trapped colloidal ring. In addition, the optical tweezers may be programmed to periodically shear the outer layer of particles and thus to explore the frequency-dependent properties of complex fluids, which represents an exciting future avenue.

We thank Thomas M. Fischer, Benjamin Dollet and Hartmut Löwen for many stimulating discussions. This research was funded by the ERC starting Grant DynaMO (No. 335040). A.O.A. acknowledges support from the "Juan de la Cierva" program (FJCI-2015-25787). J.O. and P.T. acknowledge support from from MINECO (FIS2016-78507-C2) and DURSI (2014SGR878). S.G. and S. H. L. K. acknowledge support from the Deutsche Forschungsgemeinschaft through SFB 910 (project B2).

---

\* ptierno@ub.edu

- [1] C. W. Macosko, *Rheology Principles, Measurements, and Applications* (Wiley - VCH, New York, 1994).
- [2] G. I. Taylor, Phil. Trans. R. Soc. A, **223**, 289 (1923).
- [3] M. A. Fardin, C. Perge, and N. Taberlet, Soft Matter, **10**, 3523 (2014).
- [4] G. Debrégeas, H. Tabuteau, and J.-M. di Meglio, Phys. Rev. Lett., **87**, 178305 (2001).
- [5] J. Lauridsen, G. Chanan, and M. Dennin, Phys. Rev. Lett., **93**, 018303 (2004).
- [6] D. Howell, R. P. Behringer, and C. Veje, Phys. Rev. Lett., **82**, 5241 (1999).
- [7] W. Losert, L. Bocquet, T. C. Lubensky, and J. P. Gollub, Phys. Rev. Lett., **85**, 1428 (2000).
- [8] K. A. Reddy, Y. Forterre, and O. Pouliquen, Phys. Rev. Lett., **106**, 108301 (2011).
- [9] M. R. López-González, W. M. Holmes, P. T. Callaghan, and P. J. Photinos, Phys. Rev. Lett., **93**, 268302 (2004).
- [10] A. Groisman and V. Steinberg, Phys. Rev. Lett., **77**, 1480 (1996).
- [11] J. M. White and S. J. Muller, Phys. Rev. Lett., **84**, 5130 (2000).
- [12] K. Kim, R. J. Adrian, S. Balachandar, and R. Suresh Kumar, Phys. Rev. Lett., **100**, 134504 (2008).
- [13] R. Besseling, L. Isa, E. R. Weeks, and W. C. K. Poon, Adv. Coll. Inter. Sci., **146**, 1 (2009).
- [14] X. Cheng, J. H. McCoy, J. N. Israelachvili, and I. Cohen, Science, **333**, 1276 (2011).
- [15] N. Y. C. Lin, B. M. Guy, M. Hermes, C. Ness, J. Sun, W. C. K. Poon, and I. Cohen, Phys. Rev. Lett., **115**, 228304 (2015).
- [16] D. Derks, H. Wisman, A. van Blaaderen, and A. Imhof, Journal of Physics: Condensed Matter, **16**, S3917 (2004).
- [17] I. Cohen, B. Davidovitch, A. B. Schofield, M. P. Brenner, and D. A. Weitz, Phys. Rev. Lett., **97**, 215502 (2006).
- [18] R. Besseling, E. R. Weeks, A. B. Schofield, and W. C. K. Poon, Phys. Rev. Lett., **99**, 028301 (2007).
- [19] B. B. Yellen, O. Hovorka, and G. Friedman, Proc. Natl. Acad. Sci. U.S.A., **102**, 8860 (2005).
- [20] P. Tierno, R. Muruganathan, and T. M. Fischer, Phys. Rev. Lett., **98**, 028301 (2007).
- [21] T. Bohlein, J. Mikhael, and C. Bechinger, Nat. Materials, **11**, 126 (2012).
- [22] Z. Yan, S. K. Gray, and N. F. Scherer, Nat. Commun., **5**, 3751 (2014).
- [23] I. Williams, E. C. Ogguz, P. Bartlett, H. Löwen, and C. P. Royall, Nat. Comm., **4**, 2555 (2013).
- [24] I. Williams, E. C. Ogguz, T. Speck, P. Bartlett, H. Löwen, and C. P. Royall, Nat. Phys., **12**, 98103 (2016).
- [25] See EPAPS Document No.xxxx for more details on the experimental system, the theoretical model and four video clips illustrating the particle dynamics.
- [26] A. Vanossi, N. Manini, and E. Tosatti, Proc Natl Acad Sci U.S.A., **109**, 16429 (2012).
- [27] S. Gerloff and S. H. L. Klapp, Phys. Rev. E, **94**, 062605 (2016).
- [28] W. Fornari, L. Brandt, P. Chaudhuri, C. U. Lopez, D. Mitra, and F. Picano, Phys. Rev. Lett., **116**, 018301 (2016).
- [29] S. H. L. Klapp, Y. Zeng, D. Qu, and R. von Klitzing, Phys. Rev. Lett., **100**, 118303 (2008).
- [30] M. M. Couette, Ann. Chim. Phys., **6**, 433 (1890).
- [31] The magnetic dipolar interaction energy between a pair of particles ( $i, j$ ) with moments  $m_i, m_j$  and located at a distance  $\mathbf{r}_{ij} = |\mathbf{r}_i - \mathbf{r}_j|$  is given by,  $U_d = (\mu_0/4\pi)[(\mathbf{m}_i \cdot \mathbf{m}_j)/r_{ij}^3 - 3(\mathbf{m}_i \cdot \mathbf{r}_{ij})(\mathbf{m}_j \cdot \mathbf{r}_{ij})/r_{ij}^5]$ . This potential is attractive or repulsive when these moments are parallel or perpendicular to the separation distance  $\mathbf{r}_{ij}$ . Performing a time average of the dipolar energy between two equal colloids for a magnetic field rotating in the ( $x, y$ ) plane, gives an attractive potential in this plane  $\langle U_d \rangle = -\frac{\mu_0 m^2}{8\pi(x+y)^3}$ , leading to clustering, as previously reported [20].
- [32] X. J. A. Janssen, A. J. Schellekens, K. van Ommering, L. J. van Ijzendoorn, and M. J. Prins, Biosens. Bioelectron., **24**, 1937 (2009).
- [33] A. Cebers and H. Kalis, Eur. Phys. J. E, **34**, 1292 (2011).
- [34] D. M. Mueth, G. F. Debrégeas, G. S. Karczmar, P. J. Eng, S. R. Nagel, and H. M. Jaeger, Nature, **406**, 385 (2000).
- [35] D. Fenistein, J. W. van de Meent, and M. van Hecke, Phys. Rev. Lett., **92**, 094301 (2004).
- [36] R. P. Behringer, D. Bi, B. Chakraborty, S. Henkes, and R. R. Hartley, Phys. Rev. Lett., **101**, 268301 (2008).